Tunable Microwave Single-Photon Source Based on Transmon Qubit with High Efficiency

Yu Zhou,[1,2,*] Zhihui Peng,[2,3] Yuta Horiuchi,[1] O.V. Astafiev,[4,5,6,7] and J.S. Tsai[1,2,†]

[1] *Department of Physics, Tokyo University of Science, 1-3 Kagurazaka, Shinjuku-ku, Tokyo 162-8601, Japan*
[2] *Center for Emergent Matter Science, RIKEN, 2-1 Hirosawa, Wako, Saitama 351-0198, Japan*
[3] *Key Laboratory of Low-Dimensional Quantum Structures and Quantum Control of Ministry of Education, Key Laboratory for Matter Microstructure and Function of Hunan Province, Department of Physics and Synergetic Innovation Center for Quantum Effects and Applications, Hunan Normal University, Changsha 410081, China*
[4] *Skolkovo Institute of Science and Technology, Moscow 143026, Russia*
[5] *Physics Department, Royal Holloway, University of London, Egham, Surrey TW20 OEX, United Kingdom*
[6] *National Physical Laboratory, Teddington TW11 OLW, United Kingdom*
[7] *Moscow Institute of Physics and Technology, Dolgoprudny 141700, Russia*

(Received 10 May 2019; revised manuscript received 29 November 2019; accepted 3 February 2020; published 3 March 2020)

Single-photon sources are of great interest because they are key elements in different promising applications of quantum technologies. Here we demonstrate a highly efficient tunable on-demand microwave single-photon source based on a transmon qubit with an intrinsic emission efficiency above 98%. The high efficiency ensures a negligible pure dephasing rate and the necessary conditions for generation of indistinguishable photons. We provide an extended discussion and analysis of the efficiency of the photon generation. To further experimentally confirm the single-photon property of the source, correlation functions of the emission field are also measured using linear detectors with a GPU-enhanced signal-processing technique. Our results experimentally demonstrate that frequency tunability and negligible pure dephasing rate can be achieved simultaneously and show that such a tunable single-photon source can be good for various practical applications in quantum communication, simulations and information processing in the microwave regime.

DOI: 10.1103/PhysRevApplied.13.034007

I. INTRODUCTION

Controllable single photons are an important tool used to study fundamental quantum mechanics and also for practical applications in quantum communication [1], sensing [2], simulations [3] and computing [4,5]. Single-photon sources thus have been extensively studied in optics [6,7] and great progress has been achieved [8–11]. Single-photon sources based on superconducting circuits [12–14] in the microwave regime have also attracted great interest, having a unique property—an easily achievable strong interaction with electromagnetic waves. This property allows high efficiency to be reached when generating and detecting microwave photons. There have already been some implementations of single-photon sources, which are based on cavity QED systems [15–19]. Instead of confining the photons with a fixed cavity mode, recently several single-photon sources have also been demonstrated by strong coupling to the one-dimensional (1D) continuum [20,21] to generate tunable single photons, using either flux qubits [22] or transmon qubits [23–25].

However, for many practical applications, such as boson sampling [26], the photons must be indistinguishable, which means that the pure dephasing should be suppressed [10,27,28]. For single-photon sources based on cavity QED systems, the negligible pure dephasing will be fulfilled naturally due to the coupling to a fixed cavity mode. However, for tunable single-photon sources, this can be achieved, when nearly perfect coupling to the 1D continuum is realized [29]. To achieve this goal, we use the transmon qubit for its simplicity and longer intrinsic coherence time compared with flux qubits in Ref. [22]. By careful engineering of the system, here we demonstrate a high-quality tunable on-demand microwave single-photon source based on a transmon qubit with an intrinsic emission efficiency above 98%, which not only means the nearly perfect collecting efficiency of emitted photons but also, more importantly, shows the negligible pure dephasing rate experimentally. In earlier experiments with the

*yu.zhou@riken.jp
†tsai@riken.jp

transmon qubits demonstrated in Refs. [23,24], the crucial pure dephasing rate is either not explicitly shown or not negligible. A systematic study of the single-photon source furthermore demonstrates the dynamics of the emission field and the correlation-function measurements with a GPU-enhanced signal-processing technique, which confirms the single-photon emission. The theoretical numerical calculations using the Lindblad master equation with time-dependent Hamiltonian agree very well with the experimental results. Our results show that the frequency tunability and negligible pure dephasing rate can be achieved simultaneously in experiment. A further analysis of the efficiency indicates that such a tunable single-photon source can be a good source for various practical applications in quantum optics and quantum information in the microwave regime.

II. DEVICE AND EXPERIMENT SETUP

Our single-photon source, see Fig. 1(a), consists of a transmon qubit [30] capacitively coupled to two open-ended 1D coplanar-waveguide transmission lines: one is weakly coupled to the transmon qubit to control its states (the control line) and the other is strongly coupled to the qubit for the photon emission (the emission line), similar to Ref. [22]. Here the control and emission lines are coupled through a capacitance network, which includes the shunt capacitor of the transmon qubit and capacitances from the qubit electrodes to the ground. The effective attenuation is estimated using an electromagnetic simulator to be more than 80 dB at 7 GHz and the measured attenuation in off-resonance is more than 50 dB with a probe power of −140 dBm.

The sample is fabricated using a standard fabrication technique for superconducting quantum circuits. The transmission line is made of a 50-nm-thick Nb film on an undoped silicon wafer. The qubit consisting of a dc superconducting quantum interference device (dc-SQUID) is fabricated with a standard $Al/AlO_x/Al$ shadow evaporation technique using an electron-beam evaporation system. From the measured spectrum, the maximum Josephson energy is $E_J^{\max}/h \approx 16.8$ GHz and the charging energy is $E_C/h \approx 415$ MHz, where $E_C = e^2/2C_q$ with an effective qubit capacitance of $C_q \approx 47$ fF. The qubit energy is controlled by an external magnetic field.

To study the single-photon source, the sample is cooled down to a temperature of about 20 mK in a dilution refrigerator with a microwave circuit as shown in Fig. 1(b). The sample is screened against external magnetic fields by a two-layer μ-metal and a one-layer Al shield [see the area of the magnetic shield in Fig. 1(b)]. Here the signal from the control line is strongly attenuated at different temperature stages of our dilution refrigerator to minimize the excitation of the transmon qubit by the room-temperature black-body radiation and an additional 20-dB attenuator

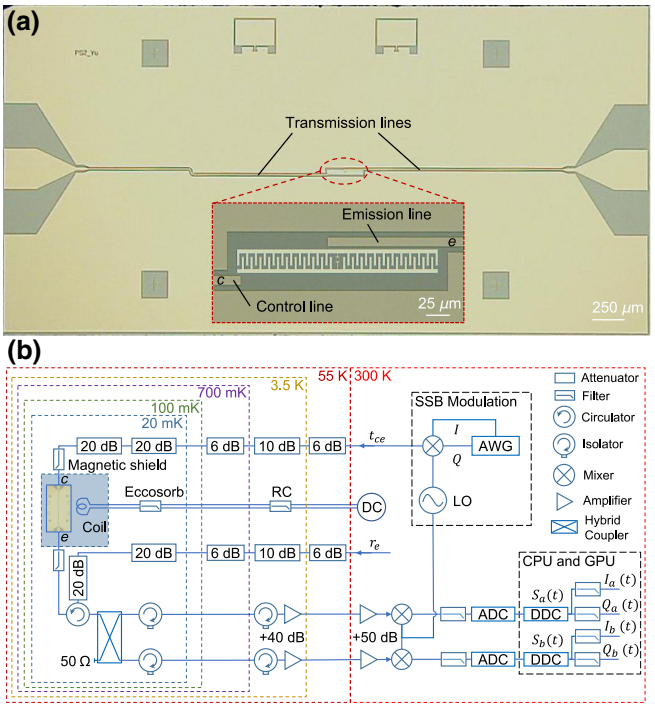

FIG. 1. (a) Optical image of the sample; the inset shows the magnified structure of the single-photon source with a transmon qubit. (b) Schematic diagram of the cryogenic and room-temperature experimental setups for both spectrum and time-domain measurements.

(giving a total attenuation of 40 dB) in the mixing chamber is used to further suppress the thermal excitations. Two high rejection low-pass filters with cut-off frequency at 8 GHz are placed at both control and emission ports of the sample to additionally protect the transmon qubit from the high-frequency radiation noise. A 4–8-GHz circulator placed in the emission line allows measurement of the reflection from the emission line, which can be used to characterize the coupling (and emission) efficiency of the single-photon source [22]. A 2–8-GHz hybrid coupler is placed at the output port working as a beam splitter in the Hanbury Brown-Twiss (HBT)-type setup [31] to show the dynamics of the emission and also the correlation functions of the emitted radiation. An idle input port of the coupler has been terminated by a 50-Ω terminator. Additional isolators situated at the mixing chamber (MC) stage protect the source from the back action of cryogenic amplifiers installed at the 4-K stage. The total gain of the output line is approximately 90 dB, including the room-temperature (RT) amplifiers. A dc bias line with a resistor-capacitor (RC) filter (at 4 K) and an Eccosorb low-pass filter (at the MC) is used for the global flux bias to tune the transition frequency of the transmon qubit.

For the time-domain and correlation-function measurements, we use the single-sideband (SSB) modulation technique with a single microwave source to stabilize the phase

in the long-lasting experiment. The single-photon emission after linear amplification is down-converted to 25 MHz and digitized with an analog-to-digital converter (ADC) at a sampling rate of 250 mega samples per second, then further processed by a CPU with a GPU-enhanced signal-processing technique to extract the quadrature amplitude $S_{a/b}(t)$ and calculate correlation functions efficiently.

Note, we use the linear detectors to carry out the correlation-function measurements [16,18,32]. Even though several microwave single-photon detectors have already been recently demonstrated [33–35], they are still far from practical applications in real-time microwave single-photon detection. So using linear detectors to carry out the correlation-function measurement is so far a more practical and general approach.

III. SPECTRUM AND EMISSION EFFICIENCY

Similar to Ref. [22], firstly, we characterize our single-photon source by measuring the transmission from control line to emission line using a vector network analyzer (VNA). The transmission is strongly enhanced, when the drive signal at ω_d is in resonance with the transmon transition frequency ω_{01}, which is a result of emission from the excited transmon qubit to the emission line under continuous microwave drive. As shown in Fig. 2(a), the single-photon source can be tuned in the range from 4 to 7 GHz.

In the observed spectrum corresponding to the system resonance frequency ω_{01} (the transition between $|0\rangle$ and $|1\rangle$ states), there are two avoided crossings due to the coupling to two-level system (TLS) defects. The large offset in flux bias is caused by the residual magnetism in cables inside the magnetic shield, which have been replaced in the later experiments. The linewidth (-3 dB in amplitude) at the sweet point with $\omega_m/2\pi = 7.062$ GHz (maximal ω_{01}) is $\Delta\omega/2\pi \approx 7$ MHz.

Next, we characterize the efficiency of the emission from the transmon qubit to the emission line. The efficiency $\eta = \Gamma_1^e/\Gamma_1$ can be defined as the ratio of the emission rate Γ_1^e over the total relaxation rate $\Gamma_1 = \Gamma_1^e + \Gamma_1^c + \Gamma_1^n$, where Γ_1^c is the relaxation rate through the emission into the control line and Γ_1^n is the nonradiative relaxation rate. We simulated our metallic structure and found from the capacitance network that the ratio of the relaxation rates to the lines Γ_1^c/Γ_1^e is $(1.0 \pm 0.3) \times 10^{-2}$, taking into account the accuracy of the derived capacitances. This means that ideally about 99% of radiation can be emitted to the emission line.

As described in Refs. [22,29], the emission amplitude of coherent radiation is determined by the expectation value of the qubit annihilation operator $\langle\sigma^-\rangle$. By solving the master equation for the two-level system under continuous drive, we find $\langle\sigma^-\rangle = -i(\Omega/2\Gamma_2)\{(1 - i\delta\omega/\Gamma_2)/[1 + (\delta\omega/\Gamma_2)^2 + \Omega^2/(\Gamma_1\Gamma_2)]\}$. Here $\delta\omega = \omega_d - \omega_{01}$ is the detuning of the drive, Ω is the Rabi frequency and $\Gamma_2 = \Gamma_1/2 + \gamma$ is the dephasing rate, which includes the pure dephasing rate γ. We can further find the reflection in the emission line r_e as

$$r_e = 1 - \frac{\Gamma_1^e}{\Gamma_2}\frac{1 - i\delta\omega/\Gamma_2}{1 + (\delta\omega/\Gamma_2)^2 + \Omega^2/(\Gamma_1\Gamma_2)}. \quad (1)$$

At the weak driving limit $\Omega \ll (\Gamma_1, \Gamma_2)$, it is simplified to

$$r_e \approx 1 - \frac{\Gamma_1^e}{\Gamma_2}\frac{1}{1 + i\delta\omega/\Gamma_2}, \quad (2)$$

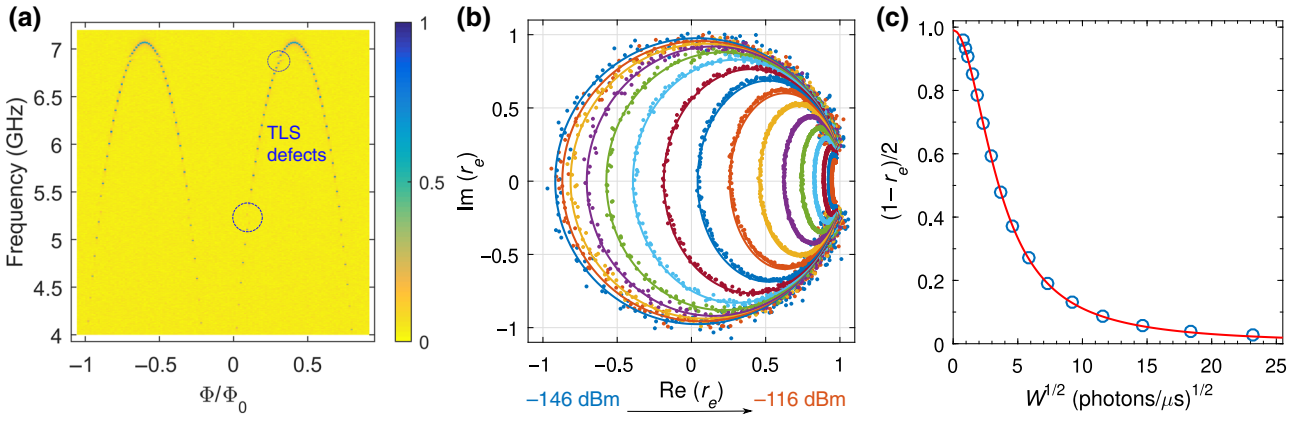

FIG. 2. (a) Normalized transmission spectrum $|t_{ce}/t_{\max}|$ versus flux bias. The large offset in flux bias is caused by the residue magnetism in cables inside the magnetic shield. There are also two avoided crossings because of the coupling to TLS defects. (b) Reflection r_e at the emission line when the transmon is biased at the sweet point. The experimental data (dots) are normalized to the background when ω_{01} is tuned far away from the sweet point. The plot is in real and imaginary coordinates at the probe power from -146 dBm (approximately 0.5 photons/μs) to -116 dBm (approximately 53.7 photons/μs) with 2 dBm/step. The solid lines represent the fitting results using Eq. (1). (c) Plot of $(1 - r_e)/2$ versus power W when $\delta\omega = 0$. The dots are data extracted from the fitting results of (b) and the solid red line is $(1 - r_e)/2 = A/(1 + kW)$, with $A = 0.991$ and a fitted factor k.

and represents a circle with a radius of $\Gamma_1^e/2\Gamma_2$. Importantly, in the ideal case with $\Gamma_1^c = \Gamma_1^n = \gamma = 0$, the radius becomes equal to one and $\eta = 1$.

As shown in Fig. 2(b), we measure the reflection r_e from the atom in the emission line (at the sweet point) with the probe power varied from a weak drive at $W = -146$ dBm up to a strong drive at -116 dBm. The data are normalized to the background measured when the qubit is tuned far away and the solid lines represent the fitting results using Eq. (1). The accuracy of the normalization procedure is subjected to uncertainty due to the uncontrolled small amplitude and the phase offset between the two separately measured signal and background traces using a VNA. We estimate that the contribution of such uncertainty to the fluctuations of the final fitted efficiency could be ± 0.01, which is consistent with the experimental observation. Fitting the experimental curves using Eq. (1) with all power traces, we find that $\eta \geq \eta' = \Gamma_1^e/2\Gamma_2 = 0.991 \pm 0.011$ in the limit of $\Omega \to 0$. Here the error mainly comes from the uncertainty of normalization and the value cannot exceed one. The efficiency value is consistent with our preliminary estimates and also confirms that there are no obvious thermal excitations, which would reduce the reflection due to the thermal population. Note that the high emission efficiency indicates that nearly all photons are emitted into the emission line and the relaxation rates Γ_1^c and Γ_1^n together with the possible pure dephasing γ are very weak. Under these conditions, the linewidth is defined by the relaxation into the emission line $\Gamma_1^e/2\pi \approx 7$ MHz and the relaxation time $T_1^e = 1/\Gamma_1^e \approx 23$ ns. Such high emission efficiency also indicates that the qubit intrinsic (nonradiative) relaxation time is much higher than 2.3 μs. For example, if the qubit intrinsic (nonradiative) relaxation time is 10 μs, it will reduce the efficiency by 23 ns/10 μs $\approx 2 \times 10^{-3}$. Such a relaxation time or an even higher value is reasonable for the transmon qubit on a silicon wafer with the fabrication techniques currently used.

IV. LIMITING FACTORS IN THE PHOTON GENERATION EFFICIENCY

Here we briefly discuss some limitations on the maximal achievable photon generation efficiency. The efficiency is affected by several factors and the coupling efficiency discussed above is important but is only one of them. In order to reach $(1 - \alpha_p)$ (where $\alpha_p \ll 1$) efficiency when preparing the excited state $|1\rangle$, one needs to drive the qubit within the time Δt, satisfying the condition $\Gamma_1^e \Delta t \approx \alpha_p$, and the required driving amplitude is $\Omega \approx \pi/\Delta t = \pi\Gamma_1^e/\alpha_p$. We also assume that the ratio of the couplings to two lines is $\alpha_c^2 = \Gamma_1^c/\Gamma_1^e$. The corresponding applied power to the control line is $W = \hbar\omega\Omega^2/\Gamma_1^c = \hbar\omega(\pi^2\Gamma_1^e/\alpha_p^2\alpha_c^2)$. There is another obvious limitation on the minimal time Δt_m allowed to prepare the excited state $|1\rangle$ by either the bandwidth of the equipment or the anharmonicity of the qubit, and thus $\alpha_p \geq \Gamma_1^e \Delta t_m$. Obviously the coupling efficiency discussed above can be presented as $\eta = 1/(1 + \alpha_c^2 + \Gamma_1^n/\Gamma_1^e)$. If we assume realistic parameters $\alpha_c^2 = 0.01$, $\alpha_p = 0.01$, and $\Delta t_m = 2$ ns, then one should make $\Gamma_1^e \leq (0.2\ \mu\text{s})^{-1}$ and $\Gamma_1^n \ll \Gamma_1^c = \alpha_c^2\Gamma_1^e = (20\ \mu\text{s})^{-1}$ to realize $\eta \approx 0.99$, which can be achieved with a typical high-quality qubit lifetime and proper engineering of the capacitance network. The total single-photon generation efficiency is then $(1 - \alpha_c^2)(1 - \alpha_p) \approx 0.98$, which includes both state preparation and emission efficiency. Substituting the parameters, we find the necessary power within the pulse to generate the photons, which is $W \approx 2 \times 10^{-10}$ W at 7 GHz; however, the total energy is only $W\Delta t_m \approx 4 \times 10^{-19}$ J. To further improve the efficiency (with the decrease of α_p and α_c^2), the power still can be increased by about 4–6 orders. Another factor to be taken into account is a direct leakage $\alpha_l = W\beta/\hbar\omega\Gamma_1^e = \pi^2\beta/\alpha_p^2\alpha_c^2$ of the coherent radiation from the control to the emission line due to the possible small stray capacitive coupling β between two lines. The factor is very weak, less than 0.01, in our current device.

Compared with our previous work [22], where the emission efficiency is 0.79 with a linewidth of 20 MHz, here we achieve a much higher emission efficiency together with a much narrower linewidth of 7 MHz. This results in a higher excited-state preparation efficiency of $1 - \alpha_p \approx 0.87$, with effective $\Delta t \approx 3$ ns and $\Gamma_1^e \approx (0.023\ \mu\text{s})^{-1}$ in the experiment. The high emission efficiency achieved in this work is a result of the properly chosen device geometry and the much longer intrinsic coherence time of our transmon qubit.

Furthermore, we also derive the emission efficiency η' over a wide frequency range for different ω_{01}, as shown on the left y axis in Fig. 3, by measuring the reflection r_e with varied probe power, similar to that in Fig. 2(b), at different flux bias points. In the figure, one can recognize the suppression of emission efficiency due to the coupling to TLS defects; see the sharp abnormal drop near the flux bias sweet point. We also estimate the effect of low-frequency $1/f$ flux noise when ω_{01} is tuned far away from the sweet point, which usually leads to a larger dephasing rate. The total dephasing rate is $\Gamma_2 = \Gamma_1/2 + \gamma$ and therefore we define $\gamma_{\text{eqv}} = (1 - \eta')\Gamma_2 = (\Gamma_1^c + \Gamma_1^n)/2 + \gamma$. The derived γ_{eqv} is shown with the right y axis in Fig. 3.

The pure dephasing rate γ due to $1/f$ flux noise with the flux noise spectral density $S_\Phi(\omega) = A_\Phi/f$ is $\gamma = \zeta(A_\Phi^{1/2}/\hbar)|\partial E_{01}/\partial\Phi|$ [36–38]. The ζ factor is a result of the integration of $1/f$ noise, which is weakly dependent on the integration limits and in our case can be approximately taken as 3.5. The dashed-dotted line on the right y axis in Fig. 3 shows the calculated γ of the $1/f$ noise with $A_\Phi^{1/2} = 1.5 \times 10^{-6}\ \Phi_0$, which is typical for properly shielded devices [39–42]. Accordingly, we also calculate the emission efficiency η' limited only by the pure dephasing γ with the same $1/f$ noise level, which is

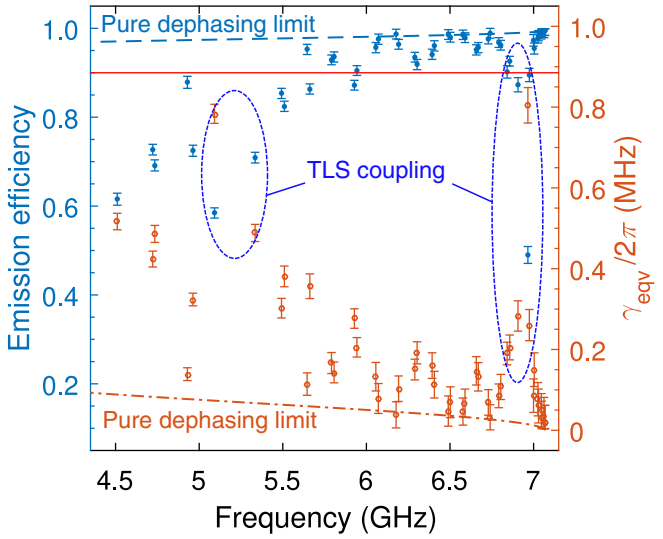

FIG. 3. Left y axis: derived emission efficiency η' over a wide range. The red line shows the position where the efficiency is 90%. The abnormal drop of η' near the flux bias sweet point is mainly caused by the coupling to the TLS defect [see the spectrum in Fig. 2(a)]. The dashed line shows maximum η' limited by the pure dephasing with $1/f$ flux noise only. The large deviation of η' from the pure dephasing limit when ω_{01} is tuned far away from the sweet point shows there exist additional dephasing sources, e.g., the fluctuations of Γ_1. Right y axis: derived equivalent dephasing rate γ_{eqv} over the same frequency range. The dashed-dotted line represents a pure dephasing rate due to the $1/f$ flux noise with spectral density $S_\Phi(\omega) = A_\Phi/f$, where $A_\Phi^{1/2} = 1.5 \times 10^{-6}\Phi_0$.

shown as a dashed line on the left y axis in Fig. 3. We see that η' and γ_{eqv} deviate more from the pure dephasing limit lines when tuned far away from the sweet point and this can be caused by the fluctuations of Γ_1 due to other reasons, e.g., frequency-dependent changes of the nonradiative relaxation rate Γ_1^n or/and the coupling capacitances to the transmission lines.

Apart from the TLS defects, we achieve emission efficiency $\eta' \geq 90\%$ over a frequency range of 1 GHz. Further improvement of the device to approach the pure dephasing limit could be made by better shielding in both the low- and high-frequency regime or an improved design with less sensitivity to the flux-dependent dephasing, such as an asymmetrical design of the dc-SQUID [42]. An additional resource for improving the state preparation efficiency can be the controllable coupling shown in Ref. [24]. However, this will require careful control of the coupling circuit to prevent further decrease of the coupling efficiency.

V. DYNAMICS OF THE EMISSION FIELD

To further study the emission dynamics we utilize an approach similar to the one used in Ref. [16]. We measure the quadrature amplitude and power of spontaneous emission from a pulse-driven qubit, namely $\langle a \rangle$ and $\langle a^\dagger a \rangle$ of the radiation mode. By using two independent detection channels a and b [43], we can average out the uncorrelated noise in each channel, which makes the measurements of microwave single photons, using linear detectors [32] and long-time averages, more efficient when compared with using just a single detection channel.

We apply a truncated Gaussian pulse $A\exp(-t^2/2\sigma^2)$ of $\sigma = 2$ ns and controlled amplitude A at the control line to coherently control the transmon qubit. We can prepare the qubit in the state $\cos(\theta_r/2)|0\rangle + \sin(\theta_r/2)|1\rangle$, where θ_r is an angle acquired in the Rabi oscillation process (Rabi angle). As shown in Figs. 4(a) and 4(d), we can observe the full dynamics of the time dependence of the emission quadrature amplitude $\langle a(t) \rangle \propto \langle S_a(t) \rangle$ and power $\langle a^\dagger(t)a(t) \rangle \propto \langle S_a^*(t)S_b(t) \rangle$, characterized by the Rabi angle θ_r with 5×10^7 ensemble averages. Instead of calculating the direct power $\langle S_a^*(t)S_a(t) \rangle$ in a single channel, we calculate the cross-power $\langle S_a^*(t)S_b(t) \rangle$ between two channels of the beam splitter [16,32], which can greatly suppress the uncorrelated noise in each channel and result in a much lower effective noise temperature (approximately 22 mK) [17].

As expected, the quadrature amplitude $\langle a(t) \rangle$ shows $(\sin\theta_r)/2$ dependence [see Fig. 4(c)], while power is $\langle a^\dagger(t)a(t) \rangle \propto \sin^2(\theta_r/2)$ [see Fig. 4(f)]. When $\langle a^\dagger(t)a(t) \rangle$ is maximal ($\theta_r = \pi$), which corresponds to the excited state $|1\rangle$ in the qubit and single-photon emission, the quadrature amplitude $\langle a(t) \rangle$ instead becomes minimal. This shows that the single-photon emission has determined photon number but uncertain phase. With short pulses, the excitation of the higher energy level $|2\rangle$ may also be possible, due to the weak anharmonicity in the transmon qubit [30,44]. In Fig. 4(c), we also show the imaginary part of $\langle a(t) \rangle$ and it cannot be calibrated to zero by adjusting the global phase [16]. The master equation calculations (see the details in Sec. VI) accounting for the energy level $|2\rangle$ well reproduce the experiment. The population of the energy level $|2\rangle$ is calculated to be about 0.003 when $\theta_r = \pi$. The decoherence decreases the fidelity of Rabi oscillations in both quadratures of amplitudes and power, when the driving amplitude is increased. Due to the limited length of the state preparation pulse by the anharmonicity of the transmon qubit (approximately 415 MHz) and the bandwidth of the 1 giga samples per second arbitrary waveform generator (AWG) (approximately 400 MHz), here the efficiency to prepare state $|1\rangle$ is approximately 0.87, which is very close to the simulated value approximately 0.88, and the total efficiency to generate a single photon is estimated to be approximately 0.86. As discussed in Sec. IV, the state preparation efficiency can be improved with better intrinsic coherence time and smaller coupling to the emission line.

To obtain the dephasing rate Γ_2 [45], we exponentially fit the decay envelope of $\langle a(t) \rangle$ when the transmon is

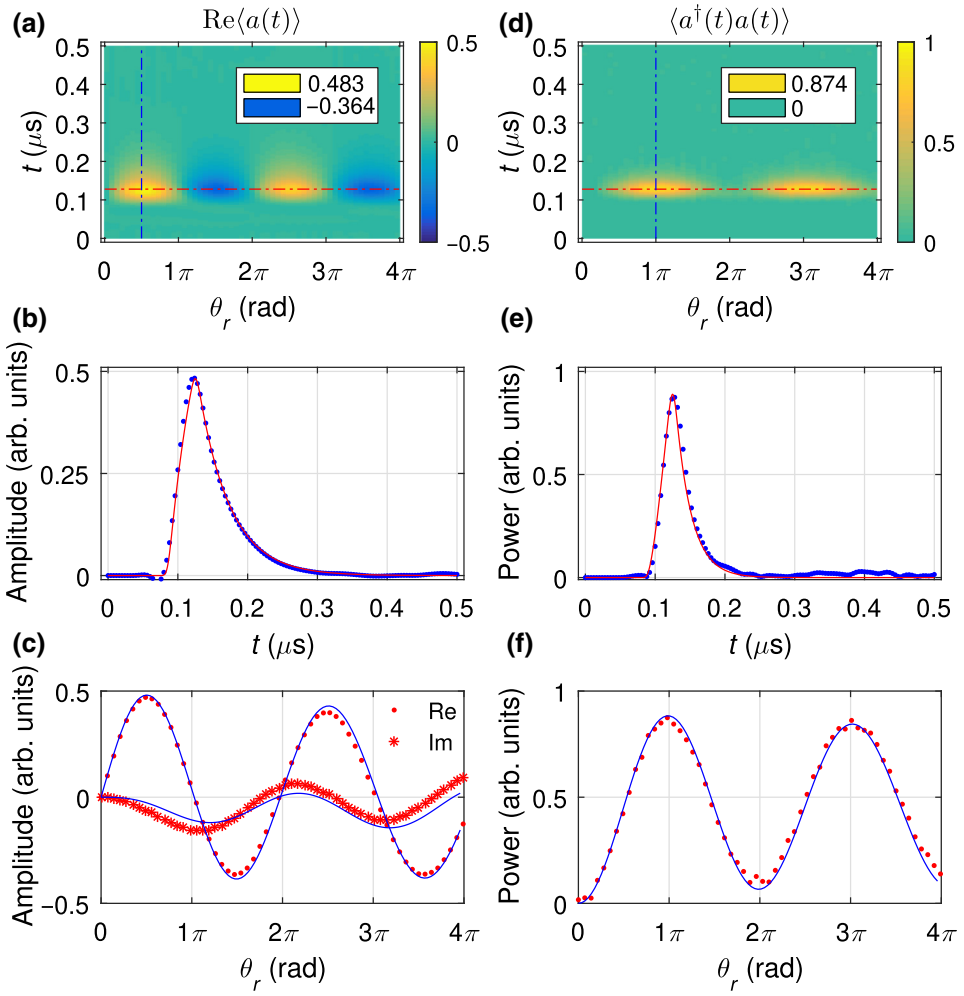

FIG. 4. (a) Time dependence of the measured quadrature amplitude (real part) of the emission field at a single channel of a beam splitter versus the Rabi angle θ_r. The legend shows colors for the maximum and minimum values. The global phase has been adjusted to minimize the imaginary part. (b) A single-amplitude trace at $\theta_r = \pi/2$, corresponding to the state $(|0\rangle + |1\rangle)/\sqrt{2}$ [the blue dashed-dotted line in (a)]. (c) The dependence of the maximum quadrature amplitude, including both real and imaginary parts, on θ_r at time t_m indicated by the red dashed-dotted line in (a). (d) Measured time dependence of cross-power between two channels for the same Rabi angle as in (a). (e) Single power trace at $\theta_r = \pi$ corresponding to the state $|1\rangle$ [blue dashed-dotted line in (d)]. (f) The dependence of maximum cross-power on θ_r at time t_m indicated by the red dashed-dotted line in (d). All the dots are experimental data, and the solid lines represent the simulation results using the model explained in Sec. VI with a finite detection bandwidth of 25 MHz.

prepared with $\theta_r = \pi/2$, as shown in Fig. 4(b), which gives us $\Gamma_2/2\pi = 3.54 \pm 0.05$ MHz. Similarly, we extract the relaxation rate $\Gamma_1/2\pi = 7.02 \pm 0.25$ MHz, which matches the linewidth measured in the spectrum, by preparing the transmon at $|1\rangle$ with $\theta_r = \pi$ and exponentially fitting the decay envelope of $\langle a^\dagger(t)a(t)\rangle$, see Fig. 4(e).

In Figs. 4(b), 4(c), 4(e), and 4(f), the experimental data are represented by dots and all solid lines represent numerical simulation results using the Lindblad master equation under a pulse drive with only two fitting parameters Γ_1 and Γ_2. The simulations here also account for the limited detection bandwidth of 25 MHz in the experiment and the theoretical temporal shapes reproduce the experimental results well, see Figs. 4(b) and 4(e). However, the limited detection bandwidth of 25 MHz does not change the decay shapes.

VI. THEORETICAL MODELING

To theoretically model the dynamics of our system, we take the Lindblad master equation approach. We consider the system as a pulse-driven, ladder-type three-level ($|0\rangle$, $|1\rangle$, and $|2\rangle$) system coupled to a transmission line.

The time-dependent system Hamiltonian in a rotating frame at drive frequency ω_d and under the rotating-wave approximation ($\hbar \equiv 1$) is

$$H(t) = \begin{pmatrix} 0 & \frac{\Omega(t)}{2} & 0 \\ \frac{\Omega(t)}{2} & \delta & \frac{\lambda\Omega(t)}{2} \\ 0 & \frac{\lambda\Omega(t)}{2} & \alpha + 2\delta \end{pmatrix}, \tag{3}$$

where $\delta = \omega_{01} - \omega_d$, $\alpha = \omega_{12} - \omega_{01}$, $\lambda = \sqrt{2}$ [30,44], and $\Omega(t)$ is a time-dependent drive strength with the Gaussian shape of $\Omega(t) = \Omega_0 \exp(-t^2/2\sigma^2)$.

The time-dependent Lindblad master equation for the density matrix ρ is

$$\dot{\rho}(t) = -\frac{i}{\hbar}[H(t), \rho(t)] + \sum_n \frac{1}{2}[2C_n\rho(t)C_n^+ - \rho(t)C_n^+C_n - C_n^+C_n\rho(t)], \tag{4}$$

where $C_n = \sqrt{\gamma_n} A_n$ are collapse operators and A_n are the operators through which the system couples to environment modes.

Specifically, here we take

$$C_1 = \sqrt{\Gamma_1}\sigma_{01}, \quad C_2 = \sqrt{\frac{\gamma}{2}}\sigma_{11}, \\ C_3 = \sqrt{2\Gamma_1}\sigma_{12}, \quad C_4 = \sqrt{\frac{\gamma}{2}}\sigma_{22}, \tag{5}$$

where $\sigma_{jk} = |j\rangle\langle k|$ with $\{|j\rangle, |k\rangle\} = \{|0\rangle, |1\rangle, |2\rangle\}$.

Now we have only modeled our system using internal system operators, which are not straightforwardly related to the photon emission. Then input-output theory [46] provides us a direct connection between the internal system operator σ_{01} and the external radiation mode operator a by $a = \sqrt{\Gamma_1}\sigma_{01}$.

For the dynamics of the emission field in both the quadrature amplitude and power, we have

$$\langle a(t)\rangle = \sqrt{\Gamma_1}\langle\sigma_{01}(t)\rangle, \tag{6}$$

$$\langle a^\dagger(t)a(t)\rangle = \Gamma_1\langle\sigma_{10}(t)\sigma_{01}(t)\rangle. \tag{7}$$

For correlation functions, there are

$$G^{(1)}(t,\tau) = \langle a^\dagger(t)a(t+\tau)\rangle \\ = \Gamma_1\langle\sigma_{10}(t)\sigma_{01}(t+\tau)\rangle, \tag{8}$$

$$G^{(2)}(t,\tau) = \langle a^\dagger(t)a^\dagger(t+\tau)a(t+\tau)a(t)\rangle \\ = \Gamma_1^2\langle\sigma_{10}(t)\sigma_{10}(t+\tau)\sigma_{01}(t+\tau)\sigma_{01}(t)\rangle. \tag{9}$$

We numerically solve the Lindblad master equation described above with real experimental parameters using QuTip [47,48] to simulate the time evolution of our system. The anharmonicity of the transmon $\alpha/2\pi \approx -415$ MHz is measured with a two-tone spectrum (not shown). $\gamma = \Gamma_2 - \Gamma_1/2$ with the fitted Γ_1 and Γ_2 as in Sec. V. The driving strength $\Omega(t)$ has a similar truncated Gaussian pulse envelope of $\sigma = 2$ ns and controlled amplitude Ω_0. We find a good match between theoretical simulations (solid lines) and experimental data (dots) in Figs. 4(c) and 4(f). Note, here, as with the infinite detection bandwidth in the simulation, the theoretical simulations can show fast dynamics inside the rising envelope of the temporal pulse shape when $\theta_r \geq \pi$, which will help us to understand the physics of the system better [49].

For correlation functions, we can also quickly calculate the two-time correlation of different operators using QuTip built-in functions, which use the quantum regression theorem [50]. The solid lines shown in Figs. 5(a)–5(c) represent the numerical calculation results with consideration of a finite detection bandwidth. We find a good agreement between simulations and experiments.

VII. CORRELATION-FUNCTION MEASUREMENT

We measure the correlation functions of the emitted photons using linear detectors [32] with the HBT setup, see Fig. 1(b), to confirm the single-photon emission of our source. Because of the near-unity collecting efficiency of the emitted photons and a greater efficient signal-processing technique used here, we see also a much better SNR in the second-order correlation-function measurement than in our previous work [22].

We generate a train of 16 single-photon pulses ($\theta_r = \pi$) with a separation of $t_p = 512$ ns ($t_p \gg 1/\Gamma_1$) between two adjacent pulses. This ensures that the transmon qubit always returns to its ground state before being excited again. The emitted photons are split into two channels by the hybrid coupler and then are amplified at both the 4-K and RT stages. Next, the signals from two channels are down-converted to intermediate frequency (IF) signals at 25 MHz and filtered by a 48-MHz low-pass filter. Finally, the IF signals are digitized by two ADCs and further processed by the CPU with a GPU-enhanced signal-processing technique to calculate the correlations between the two quadrature amplitudes $S_a(t)$ and $S_b(t)$.

For calculation of the correlation functions, we follow the same method as in Ref. [16,32]:

$$\Gamma^{(1)}(\tau) = \int \langle S_a^*(t)S_b(t+\tau)\rangle dt, \tag{10}$$

which measures the first-order cross-correlation of the signals $S_a(t)$ and $S_b(t)$:

$$\Gamma^{(2)}(\tau) = \int \langle S_a^*(t)S_a^*(t+\tau)S_b(t+\tau)S_b(t)\rangle dt, \tag{11}$$

which measures the quasi-auto-correlation of the cross-power $S_a^*(t)S_b(t)$ and serves as a measurement of the second-order correlation function only in the HBT-like setup with an idle input port in vacuum.

To remove the correlated noise background [$\Gamma_{bg}^{(1)}(\tau)$ and $\Gamma_{bg}^{(2)}(\tau)$], each signal trace is immediately followed by a trace of noise background, when the photon source is not excited. Signal traces and noise background traces are calculated and averaged in the same way to get the correlation function. Then, we can obtain the correlation function of the emitted photons by

$$G^{(1)}(\tau) \propto \Gamma^{(1)}(\tau) - \Gamma_{bg}^{(1)}(\tau), \tag{12}$$

$$G^{(2)}(\tau) \propto \Gamma^{(2)}(\tau) - \Gamma_{bg}^{(2)}(\tau). \tag{13}$$

For $G^{(1)}(\tau)$, the trace (dots) shown in Fig. 5(a) is averaged by 5×10^7 trains of 16 photons with a specific prepared

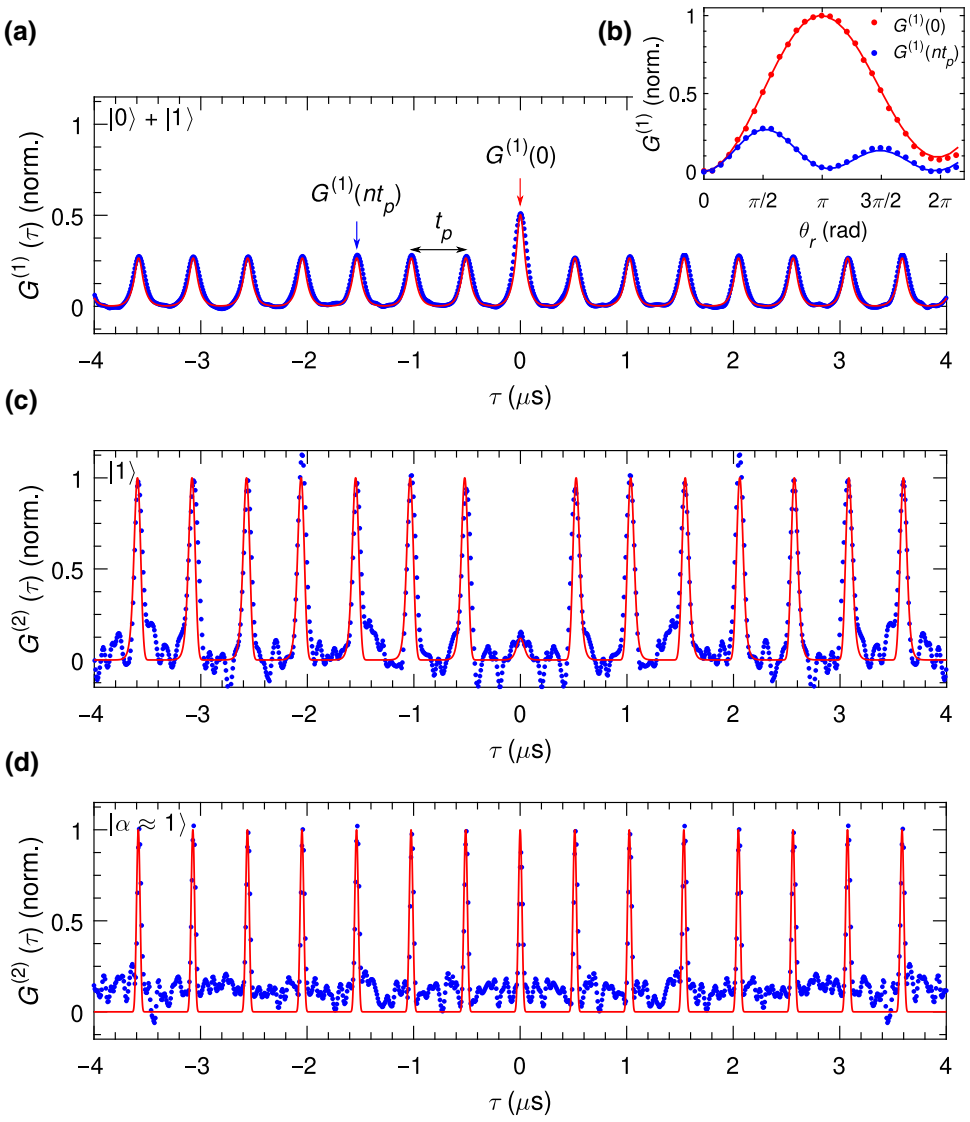

FIG. 5. (a) The time dependence of the first-order correlation function $G^{(1)}(\tau)$ for $(|0\rangle + |1\rangle)/\sqrt{2}$. (b) The dependence of a center peak $G^{(1)}(0)$ and a side peak $G^{(1)}(nt_p)$ on the prepared Rabi angle θ_r. (c) The measured second-order correlation function $G^{(2)}(\tau)$ for the state $|1\rangle$. (d) The measured second-order correlation function $G^{(2)}(\tau)$ for the coherent state $|\alpha \approx 1\rangle$. All the dots represent experimental data and solid lines represent theoretical calculations including the effect of limited detection bandwidth in the experiment.

state. Figure 5(b) shows the dependence of $G^{(1)}(0)$ and $G^{(1)}(nt_p)$ on the Rabi angle θ_r. The center peak $G^{(1)}(0) \propto \langle a^\dagger a\rangle$ measures the average emitted number of photons. As photons generated in different pulses are not correlated ($t_p \gg 1/\Gamma_1$), $G^{(1)}(nt_p) \propto \langle a^\dagger\rangle\langle a\rangle$. Here, the solid lines represent simulation results using the master equation (see Sec. VI) with a finite detection bandwidth of 20 MHz. The damping of the oscillation is mainly due to the decoherence. We see an excellent agreement between our theoretical calculations and experiment results.

For $G^{(2)}(\tau)$, the measurement in the microwave regime is technically difficult due to the very poor SNR, which needs extremely large averaging ($> 10^9$) to achieve a reasonable confidence in experimental data. Instead of using the field-programmable gate array (FPGA) to realize real-time signal processing [16,18], here we take an intermediate approach using 1792 compute unified device architecture (CUDA) cores in the GPU to realize parallel signal processing, which creates an increase in speed of 4× when compared to solely using one Xeon CPU of six cores. The approach demonstrated here is not as efficient as the FPGA but easier to achieve and also has higher flexibility. The trace (dots) in Fig. 5(c) is averaged 4.8×10^9 times within 34 h, corresponding to approximately 36 TB of data processed in total. The data have been normalized to the average peak height of $G^{(2)}(nt_p)$ for state $|1\rangle$ ($\theta_r = \pi$) [16]. We see a strongly suppressed center peak $G^{(2)}(0) \approx 0.15 \ll 1$, which is limited by $\Gamma_1 T_{\mathrm{FWHM}}$, where T_{FWHM} is the length of the state preparation pulse [51]. This result shows clear evidence of the single-photon emission from our source. Here the detection bandwidth is set at 12.5 MHz to suppress the noise outside of the signal bandwidth approximately 7 MHz. The solid line represents the result of the master equation simulation with the experimental detection bandwidth and $G^{(2)}(0) \approx 0.1$ is very close to the experimental value.

To further confirm our experimental results, we carry out another experiment for comparison. We directly generate a short coherent Gaussian pulse with $\sigma = 8$ ns and the power is calibrated to make sure that the average photon number inside the pulse is approximately one. Then we measure the second-order correlation function $G^{(2)}(\tau)$ of this coherent state $|\alpha \approx 1\rangle$ with 4×10^9 averages, see Fig. 5(d). As expected, we observe $G^{(2)}(0) \approx 0.9$ at $\tau = 0$, which is in significant contrast to the Fock state $|1\rangle$. The red line is the theoretical calculation with a real pulse temporal shape and a finite detection bandwidth. The noise background is slightly higher than Fig. 5(c) because of the broadband noise existing in this particular experimental setup with a transmission line.

Note, here, we demonstrate the antibunching of photons emitted from our source. In further experiments, we can also demonstrate indistinguishability of photons, using the Hong-Ou-Mandel (HOM) effect [27,52]. The demonstration of the HOM effect from the same single-photon source in the microwave regime is challenging because of the difficulty to introduce the large time delay (hundreds of nanoseconds) at cryogenic temperatures. Due to the strong coupling to the 1D continuum, we should have negligible pure dephasing ($\gamma \approx 0$) [29] and $2\Gamma_2/\Gamma_1 = 1$. If this condition is satisfied, perfect two-photon interference can be expected [27,28]. Here, in our source, $2\Gamma_2/\Gamma_1 \approx 1$, which indicates good two-photon interference. Thus, higher emission efficiency η' also means better indistinguishability of emitted photons from the source, which is crucial for practical applications.

VIII. CONCLUSION

In conclusion, we demonstrate a highly efficient tunable microwave single-photon source based on a transmon qubit with an intrinsic emission efficiency of approximately 0.99 ± 0.01. Considering the state preparation efficiency of approximately 0.87, the total single-photon generation efficiency is approximately 0.86 ± 0.01. The single-photon emission of our source is also confirmed by correlation-function measurements using a GPU-enhanced signal-processing technique. In this work, we have substantially improved the performance of a tunable microwave single-photon source. The achieved emission efficiency above 98% is a result of the negligible pure dephasing rate, which is strong evidence that the emitted photons are indistinguishable. Further analysis also shows that the state preparation efficiency can be further improved with better intrinsic coherence time (e.g., $T_1^n \sim 20\ \mu$s) and smaller coupling to the emission line (e.g., $T_1^e \sim 0.2\ \mu$s). Our result shows that such a tunable microwave single-photon source using a waveguide scheme can be good for various practical applications in quantum communication, simulation and information processing in the microwave regime.

ACKNOWLEDGMENTS

Y. Zhou thanks D. K. Zhang, R. Wang, N. Lambert and A. Miranowicz for valuable discussion, H. Mukai for help in the experimental setup and K. Kusuyama for help in fabrication. This work was supported by CREST, JST (Grant No. JPMJCR1676), the New Energy and Industrial Technology Development Organization (NEDO), and the ImPACT Program of Council for Science, Technology and Innovation (Cabinet Office, Government of Japan). Z.H.P. is supported by NSFC under Grant No. 61833010 and Hunan Province Science and Technology Innovation Platform and Talent Plan (Excellent Talent Award) under Grant No. 2017XK2021. O.V.A. is supported by the Russian Science Foundation (Grant No. 16-12-00070).

[1] H. J. Kimble, The quantum internet, Nature **453**, 1023 (2008).
[2] C. L. Degen, F. Reinhard, and P. Cappellaro, Quantum sensing, Rev. Mod. Phys. **89**, 035002 (2017).
[3] I. M. Georgescu, S. Ashhab, and F. Nori, Quantum simulation, Rev. Mod. Phys. **86**, 153 (2014).
[4] E. Knill, R. Laflamme, and G. J. Milburn, A scheme for efficient quantum computation with linear optics, Nature **409**, 46 (2001).
[5] P. Kok, W. J. Munro, K. Nemoto, T. C. Ralph, J. P. Dowling, and G. J. Milburn, Linear optical quantum computing with photonic qubits, Rev. Mod. Phys. **79**, 135 (2007).
[6] B. Lounis and M. Orrit, Single-photon sources, Rep. Prog. Phys. **68**, 1129 (2005).
[7] M. D. Eisaman, J. Fan, A. Migdall, and S. V. Polyakov, Invited review article: Single-photon sources and detectors, Rev. Sci. Instrum. **82**, 071101 (2011).
[8] X. Ding, Y. He, Z.-C. Duan, N. Gregersen, M.-C. Chen, S. Unsleber, S. Maier, C. Schneider, M. Kamp, S. Höfling, C.-Y. Lu, and J.-W. Pan, On-Demand Single Photons with High Extraction Efficiency and Near-Unity Indistinguishability from a Resonantly Driven Quantum dot in a Micropillar, Phys. Rev. Lett. **116**, 020401 (2016).
[9] N. Somaschi, V. Giesz, L. De Santis, J. C. Loredo, M. P. Almeida, G. Hornecker, S. L. Portalupi, T. Grange, C. Antón, J. Demory, C. Gómez, I. Sagnes, N. D. Lanzillotti-Kimura, A. Lemaítre, A. Auffeves, A. G. White, L. Lanco, and P. Senellart, Near-optimal single-photon sources in the solid state, Nat. Photonics **10**, 340 (2016).
[10] P. Senellart, G. Solomon, and A. White, High-performance semiconductor quantum-dot single-photon sources, Nat. Nanotechnol. **12**, 1026 (2017).
[11] L. Schweickert, K. D. Jöns, K. D. Zeuner, S. F. Covre da Silva, H. Huang, T. Lettner, M. Reindl, J. Zichi, R. Trotta, A. Rastelli, and V. Zwiller, On-demand generation of background-free single photons from a solid-state source, Appl. Phys. Lett. **112**, 093106 (2018).
[12] J. Q. You and F. Nori, Superconducting circuits and quantum information, Phys. Today **58**, 42 (2005).
[13] M. H. Devoret and R. J. Schoelkopf, Superconducting circuits for quantum information: An outlook, Science **339**, 1169 (2013).

[14] X. Gu, A. F. Kockum, A. Miranowicz, Y.-X. Liu, and F. Nori, Microwave photonics with superconducting quantum circuits, Phys. Rep. **718-719**, 1 (2017).

[15] A. A. Houck, D. I. Schuster, J. M. Gambetta, J. A. Schreier, B. R. Johnson, J. M. Chow, L. Frunzio, J. Majer, M. H. Devoret, S. M. Girvin, and R. J. Schoelkopf, Generating single microwave photons in a circuit, Nature **449**, 328 (2007).

[16] D. Bozyigit, C. Lang, L. Steffen, J. M. Fink, C. Eichler, M. Baur, R. Bianchetti, P. J. Leek, S. Filipp, M. P. da Silva, A. Blais, and A. Wallraff, Antibunching of microwave-frequency photons observed in correlation measurements using linear detectors, Nat. Phys. **7**, 154 (2011).

[17] D. Bozyigit, C. Lang, L. Steffen, J. M. Fink, C. Eichler, M. Baur, R. Bianchetti, P. J. Leek, S. Filipp, A. Wallraff, M. P. Da Silva, and A. Blais, Correlation measurements of individual microwave photons emitted from a symmetric cavity, J. Phys. Conf. Ser. **264**, 012024 (2011).

[18] C. Lang, C. Eichler, L. Steffen, J. M. Fink, M. J. Woolley, A. Blais, and A. Wallraff, Correlations, indistinguishability and entanglement in Hong–Ou–Mandel experiments at microwave frequencies, Nat. Phys. **9**, 345 (2013).

[19] M. Pechal, L. Huthmacher, C. Eichler, S. Zeytinoglu, A. A. Abdumalikov, S. Berger, A. Wallraff, and S. Filipp, Microwave-Controlled Generation of Shaped Single Photons in Circuit Quantum Electrodynamics, Phys. Rev. X **4**, 041010 (2014).

[20] J. Lindkvist and G. Johansson, Scattering of coherent pulses on a two-level system–single-photon generation, New J. Phys. **16**, 055018 (2014).

[21] D. Roy, C. M. Wilson, and O. Firstenberg, Colloquium: Strongly interacting photons in one-dimensional continuum, Rev. Mod. Phys. **89**, 021001 (2017).

[22] Z. H. Peng, S. E. de Graaf, J. S. Tsai, and O. V. Astafiev, Tuneable on-demand single-photon source in the microwave range, Nat. Commun. **7**, 12588 (2016).

[23] M. Pechal, J.-C. Besse, M. Mondal, M. Oppliger, S. Gasparinetti, and A. Wallraff, Superconducting Switch for Fast On-Chip Routing of Quantum Microwave Fields, Phys. Rev. Appl. **6**, 024009 (2016).

[24] P. Forn-Diaz, C. W. Warren, C. W. S. Chang, A. M. Vadiraj, and C. M. Wilson, On-Demand Microwave Generator of Shaped Single Photons, Phys. Rev. Appl. **8**, 054015 (2017).

[25] S. Gasparinetti, M. Pechal, J.-C. Besse, M. Mondal, C. Eichler, and A. Wallraff, Correlations and Entanglement of Microwave Photons Emitted in a Cascade Decay, Phys. Rev. Lett. **119**, 140504 (2017).

[26] S. Aaronson and A. Arkhipov, The computational complexity of linear optics, Theory Comput. **9**, 143 (2013).

[27] C. Santori, D. Fattal, J. Vučković, G. S. Solomon, and Y. Yamamoto, Indistinguishable photons from a single-photon device, Nature **419**, 594 (2002).

[28] J. Bylander, I. Robert-Philip, and I. Abram, Interference and correlation of two independent photons, Eur. Phys. J. D **22**, 295 (2003).

[29] O. Astafiev, A. M. Zagoskin, A. A. Abdumalikov, Y. A. Pashkin, T. Yamamoto, K. Inomata, Y. Nakamura, and J. S. Tsai, Resonance fluorescence of a single artificial atom, Science **327**, 840 (2010).

[30] J. Koch, T. M. Yu, J. Gambetta, A. A. Houck, D. I. Schuster, J. Majer, A. Blais, M. H. Devoret, S. M. Girvin, and R. J. Schoelkopf, Charge-insensitive qubit design derived from the cooper pair box, Phys. Rev. A **76**, 042319 (2007).

[31] R. H. Brown and R. Q. Twiss, Correlation between photons in two coherent beams of light, Nature **177**, 27 (1956).

[32] M. P. da Silva, D. Bozyigit, A. Wallraff, and A. Blais, Schemes for the observation of photon correlation functions in circuit QED with linear detectors, Phys. Rev. A **82**, 043804 (2010).

[33] K. Inomata, Z. Lin, K. Koshino, W. D. Oliver, J.-S. Tsai, T. Yamamoto, and Y. Nakamura, Single microwave-photon detector using an artificial Λ-type three-level system, Nat. Commun. **7**, 12303 (2016).

[34] S. Kono, K. Koshino, Y. Tabuchi, A. Noguchi, and Y. Nakamura, Quantum non-demolition detection of an itinerant microwave photon, Nat. Phys. **14**, 546 (2018).

[35] J.-C. Besse, S. Gasparinetti, M. C. Collodo, T. Walter, P. Kurpiers, M. Pechal, C. Eichler, and A. Wallraff, Single-Shot Quantum Nondemolition Detection of Individual Itinerant Microwave Photons, Phys. Rev. X **8**, 021003 (2018).

[36] O. Astafiev, Y. A. Pashkin, Y. Nakamura, T. Yamamoto, and J. S. Tsai, Quantum Noise in the Josephson Charge Qubit, Phys. Rev. Lett. **93**, 267007 (2004).

[37] G. Ithier, E. Collin, P. Joyez, P. J. Meeson, D. Vion, D. Esteve, F. Chiarello, A. Shnirman, Y. Makhlin, J. Schriefl, and G. Schön, Decoherence in a superconducting quantum bit circuit, Phys. Rev. B **72**, 134519 (2005).

[38] A. Shnirman, Y. Makhlin, and G. Schön, Noise and decoherence in quantum two-level systems, Phys. Scr. **2002**, 147 (2002).

[39] F. Yoshihara, K. Harrabi, A. O. Niskanen, Y. Nakamura, and J. S. Tsai, Decoherence of Flux Qubits due to $1/f$ Flux Noise, Phys. Rev. Lett. **97**, 167001 (2006).

[40] K. Kakuyanagi, T. Meno, S. Saito, H. Nakano, K. Semba, H. Takayanagi, F. Deppe, and A. Shnirman, Dephasing of a Superconducting Flux Qubit, Phys. Rev. Lett. **98**, 047004 (2007).

[41] R. C. Bialczak, R. McDermott, M. Ansmann, M. Hofheinz, N. Katz, E. Lucero, M. Neeley, A. D. O'Connell, H. Wang, A. N. Cleland, and J. M. Martinis, $1/f$ Flux Noise in Josephson Phase Qubits, Phys. Rev. Lett. **99**, 187006 (2007).

[42] M. D. Hutchings, J. B. Hertzberg, Y. Liu, N. T. Bronn, G. A. Keefe, M. Brink, J. M. Chow, and B. L. T. Plourde, Tunable Superconducting Qubits With Flux-Independent Coherence, Phys. Rev. Appl. **8**, 044003 (2017).

[43] E. P. Menzel, F. Deppe, M. Mariantoni, M. A. Araque Caballero, A. Baust, T. Niemczyk, E. Hoffmann, A. Marx, E. Solano, and R. Gross, Dual-Path State Reconstruction Scheme for Propagating Quantum Microwaves and Detector Noise Tomography, Phys. Rev. Lett. **105**, 100401 (2010).

[44] F. Motzoi, J. M. Gambetta, P. Rebentrost, and F. K. Wilhelm, Simple Pulses for Elimination of Leakage in Weakly Nonlinear Qubits, Phys. Rev. Lett. **103**, 110501 (2009).

[45] A. A. Abdumalikov, O. V. Astafiev, Y. A. Pashkin, Y. Nakamura, and J. S. Tsai, Dynamics of Coherent and Incoherent Emission from an Artificial Atom in a 1D Space, Phys. Rev. Lett. **107**, 043604 (2011).

[46] D. Walls and G. Milburn, *Quantum Optics* (Springer, Berlin, Heidelberg, 2008).

[47] J. Johansson, P. Nation, and F. Nori, QuTiP: An open-source Python framework for the dynamics of open quantum systems, Comput. Phys. Commun. **183**, 1760 (2012).

[48] J. Johansson, P. Nation, and F. Nori, QuTiP 2: A Python framework for the dynamics of open quantum systems, Comput. Phys. Commun. **184**, 1234 (2013).

[49] K. A. Fischer, L. Hanschke, M. Kremser, J. J. Finley, K. Müller, and J. Vučković, Pulsed Rabi oscillations in quantum two-level systems: Beyond the area theorem, Quantum Sci. Technol. **3**, 014006 (2018).

[50] C. Gardiner and P. Zoller, *Quantum Noise: A Handbook of Markovian and Non-Markovian Quantum Stochastic Methods with Applications to Quantum Optics*, Springer Series in Synergetics (Springer, Berlin, Heidelberg, 2004).

[51] K. A. Fischer, K. Müller, K. G. Lagoudakis, and J. Vučković, Dynamical modeling of pulsed two-photon interference, New J. Phys. **18**, 113053 (2016).

[52] C. K. Hong, Z. Y. Ou, and L. Mandel, Measurement of Subpicosecond Time Intervals between two Photons by Interference, Phys. Rev. Lett. **59**, 2044 (1987).